Nano Research

Open Access

Research Article

Band and defect engineering in solution-processed nanocrystal building blocks to promote transport properties in nanomaterials: The case of thermoelectric Cu_3SbSe_4

Shanshan Xiao[1], Mingjun Zhao[1], Mingquan Li[1], Shanhong Wan[1], Aziz Genç[2], Lulu Huang[3], Lei Chen[4], Yu Zhang[5], Maria Ibáñez[6], Khak Ho Lim[7,8] ✉, Min Hong[4] ✉, Yu Liu[1] ✉, and Andreu Cabot[9,10] ✉

[1] *School of Chemistry and Chemical Engineering, Hefei University of Technology, Hefei 230009, China*
[2] *Cardiff Catalysis Institute, School of Chemistry, Cardiff University, Cardiff CF10 3AT, UK*
[3] *School of Materials Science and Engineering, Hefei University of Technology, Hefei 230009, China*
[4] *Centre for Future Materials and School of Engineering, University of Southern Queensland, Springfield Central, Queensland 4300, Australia*
[5] *Institute of Wenzhou-Zhejiang University, Wenzhou 325028, China*
[6] *Institute of Science and Technology Austria (ISTA), Am Campus 1, Klosterneuburg 3400, Austria*
[7] *College of Chemical and Biological Engineering, Zhejiang University, Hangzhou 310007, China*
[8] *Institute of Zhejiang University-Quzhou, Quzhou 324000, China*
[9] *Catalonia Institute for Energy Research-IREC, Sant Adrià de Besòs, Barcelona 08930, Spain*
[10] *Catalan Institution for Research and Advanced Studies (ICREA), Pg. Lluís Companys 23, Barcelona, Catalonia 08010, Spain*

Cite this article: *Nano Research*, **2025**, *18*, 94907072. https://doi.org/10.26599/NR.2025.94907072

ABSTRACT: The development of cost-effective and high-performance thermoelectric (TE) materials faces significant challenges, particularly in improving the properties of promising copper-based TE materials such as Cu_3SbSe_4, which are limited by their poor electrical conductivity. This study presents a detailed comparative analysis of three strategies to promote the electrical transport properties of Cu_3SbSe_4 through Sn doping: conventional Sn atomic doping, surface treatment with SnSe molecular complexes, and blending with SnSe nanocrystals to form nanocomposites, all followed by annealing and hot pressing under identical conditions. Our results reveal that a surface treatment using SnSe molecular complexes significantly enhances TE performance over atomic doping and nanocomposite formation, achieving a power factor of 1.1 $mW \cdot m^{-1} \cdot K^{-2}$ and a maximum dimensionless figure of merit zT value of 0.80 at 640 K, representing an excellent performance among Cu_3SbSe_4-based materials produced via solution-processing methods. This work highlights the effectiveness of surface engineering in optimizing the transport properties of nanostructured materials, demonstrating the versatility and cost-efficiency of solution-based technologies in the development of advanced nanostructured materials for application in the field of TE among others.

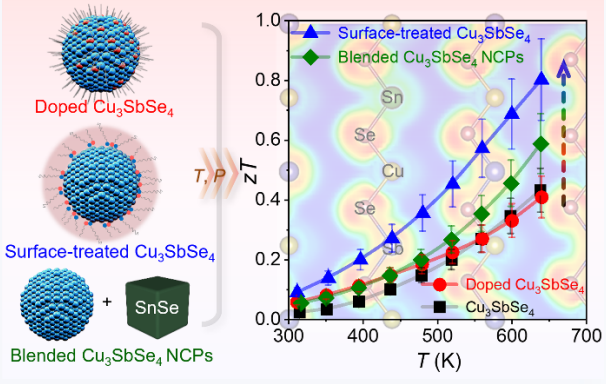

KEYWORDS: Cu_3SbSe_4 nanocrystal, solution processing, surface-treatment, band engineering, thermoelectricity

1 Introduction

Thermoelectric (TE) materials, which convert heat into electricity and vice versa, are essential components in space exploration devices, compact cooling systems for 5G networks, and body heat self-powering technologies integral to the Internet of Things (IoT) among numerous other varied temperature control, cooling, and energy harvesting applications [1, 2]. The efficiency of these materials is quantified by a dimensionless figure of merit, $zT = \sigma S^2 T/\kappa_{tot}$, where σ represents electrical conductivity, S is the Seebeck coefficient, T denotes absolute temperature, and κ_{tot} represents total thermal conductivity [3–5]. The interdependence of these parameters complicates efforts to optimize zT, as improving σ can

Received: September 2, 2024; **Revised:** September 29, 2024
Accepted: October 11, 2024

✉Address correspondence to Yu Liu, yliu@hfut.edu.cn; Min Hong, min.hong@unisq.edu.au; Khak Ho Lim, khlim@zju.edu.cn; Andreu Cabot, acabot@irec.cat

inadvertently decrease S and increase κ_{tot}, thereby reducing overall material efficiency. To address this challenge, strategies have been developed, including incorporating nanostructured interfaces to reduce phonon transmission without impeding electronic transport and selectively doping materials to manipulate carrier concentrations and mobility [6–8]. These approaches aim to decouple the thermal and electrical properties of materials, thereby enabling the practical realization of high-performance TE systems.

Different TE materials are used depending on the temperature range. Lead chalcogenides are typically used for applications in the mid-temperature range [7, 9–14], whereas Bi_2Te_3-based compounds predominate in room-temperature TE devices [15–19]. Despite their proven efficacy, these materials are encumbered by significant drawbacks, notably high costs and considerable health and environmental hazards due to the use of scarce and toxic elements such as Te and Pb. These limitations have driven extensive research efforts to identify and develop alternative materials composed of abundant and non-toxic elements. At the same time, next-generations of TE devices should be based on more sustainable processing approaches, beyond the energy- and labor-intensive technologies currently used for the fabrication of TE devices. Within this framework, Cu-based TE materials, distinguished by the relative abundance and reduced toxicity of their elements along with their straightforward preparation potentially using solution-based processes, have rapidly emerged as formidable contenders for supplanting lead-based compounds in mid-temperature applications [20–22].

Binary copper chalcogenides, such as Cu_2X (X = S, Se, and Te), have been extensively studied for their extraordinary TE performance, though their stability remains uncertain [23–28]. In parallel, a much less studied category of diamond-like structured ternary and multinary compounds, including Cu_2SnSe_3 [29, 30], $CuGaTe_2$ [31, 32], $Cu_2ZnGeSe_4$ [33], Cu_3SbSe_4 [34, 35], etc., has garnered significant attention due to their improved stability and notable TE properties. Among these, Cu_3SbSe_4, a semiconductor with a relatively small bandgap of 0.29 eV, has emerged as particularly promising [36]. First-principles calculations of impurity formation energies in Cu_3SbSe_4 reveal that this material typically behaves as a p-type semiconductor behavior, attributed to the low formation energy associated with Cu vacancies. At the same time, the low energy required for Sb substitution makes it the most favorable site for doping [37, 38]. Experimental research aligns with these theoretical predictions, showing that to enhance the generally poor electrical transport performance, effective doping primarily involves acceptor doping at the Sb site. Elements from groups IIIA and IVA, such as Sn [34], Ge [39], Al [40], Pb [41], In [40], and Ga [40], as well as d-block elements like Ti [42] and Ni [43], have been particularly effective in enhancing TE performance through substitutional doping at the Sb site.

Among various strategies employed to enhance the electrical performance of Cu_3SbSe_4, p-type doping with Sn at the Sb site has proven to be the most effective strategy, significantly modifying the band structure (Fig. 1(a)) [34, 35, 44, 45]. This is attributed to the structural similarities but differential valence between Sn and Sb, which ensure nearly 100% doping efficiency [34]. This large efficiency allows adjusting the charge carrier concentration in the range from 10^{18} to 10^{20} cm^{-3}, thereby significantly enhancing σ. Moreover, theoretical calculations suggest that Sn doping also elevates the effective mass (m_d^*) of holes, which substantially boosts the power factor (PF = σS^2), doubling the maximum zT value [34, 44, 45].

The phase diagram for the Cu-Sb-Se system demonstrates that, at a Cu content of 37.5%, stoichiometric Cu_3SbSe_4 is formed (Fig. S1 in the Electronic Supplementary Material (ESM)). This phase possesses a liquid phase threshold temperature of approximately 403 °C [46]. Consequently, the maximum testing and application temperatures for bulk Cu_3SbSe_4 are consistently maintained below 673 K in previous studies, due to the material's decomposition into three distinct phases at temperatures exceeding its stability limit of approximately 390 °C [40–42, 44, 47, 48]. Thermogravimetric analysis (TGA) shows that Cu_3SbSe_4 doped with a proper amount of Sn exhibits reduced weight loss at elevated temperatures (Fig. 1(b)), indicating enhanced stability compared to pristine Cu_3SbSe_4. This stability enhancement is primarily attributed to the substitution, which establishes a more stable chemical framework and strengthens the Sn–Se and neighboring Cu–Se bonds, thereby enhancing their covalent characteristics and requiring more energy to disrupt (Fig. 1(c)) [45]. Consequently, Sn doping also limits the volatilization of Se. As shown in the inset of Fig. 1(b), the unit cell of Sn-doped Cu_3SbSe_4, which features a tetragonal structure with Cu atoms occupying two distinct lattice positions (Cu_1 and Cu_2), comprises a network of tetrahedrally coordinated Sb and Se bonds, with Sn atoms incorporated at the Sb sites.

Given the significant impact of Sn in the Cu_3SbSe_4 system, investigating alternative strategies for incorporating this element, beyond conventional doping, holds interest for both deepening our understanding of Sn's role within the material and exploring potentially more effective introduction strategies. In this study, a high-yield and scalable bottom-up approach to produce Cu_3SbSe_4 nanocrystals (NCs) was studied in detail. Subsequently, three distinct Sn introduction strategies were investigated: conventional doping, surface treatment using SnSe molecular complexes, and production of nanocomposites (NCPs) by blending Cu_3SbSe_4 and SnSe NCs, each of them subsequently undergoing annealing and hot pressing under identical conditions. These approaches enable a comprehensive exploration and discussion of the significant impact of Sn on the charge and thermal transport mechanisms within Cu_3SbSe_4. Notably, the matrix treated with molecular complexes exhibits superior TE performance compared to other strategies (Fig. 1(d)), prompting a detailed analysis and investigation of the microstructure to better understand the observed enhancements.

2 Results and discussion

2.1 NC properties and pellet consolidation

Cu_3SbSe_4 NCs were synthesized following a scaled-up version of a previously reported method [35, 41]. Briefly, Se powder was dissolved in oleylamine (OLA) and 1-dodecanethiol (DDT), and the solution was injected into a preheated mixture of copper(I) chloride (CuCl) and antimony(III) chloride ($SbCl_3$) (see details in the ESM). This protocol facilitated a high batch-to-batch reproducibility and achieved a material yield of ca. 94%. Following this approach, Sn-doped Cu_3SbSe_4 NCs (doped Cu_3SbSe_4) were produced by substituting the corresponding amount of $SbCl_3$ with tin(II) chloride dihydrate ($SnCl_2{\cdot}2H_2O$), maintaining consistent synthesis conditions.

The blended Cu_3SbSe_4 NCPs were produced by wetting 1.5 g of dried and ligand-free Cu_3SbSe_4 NCs with the desired amounts of

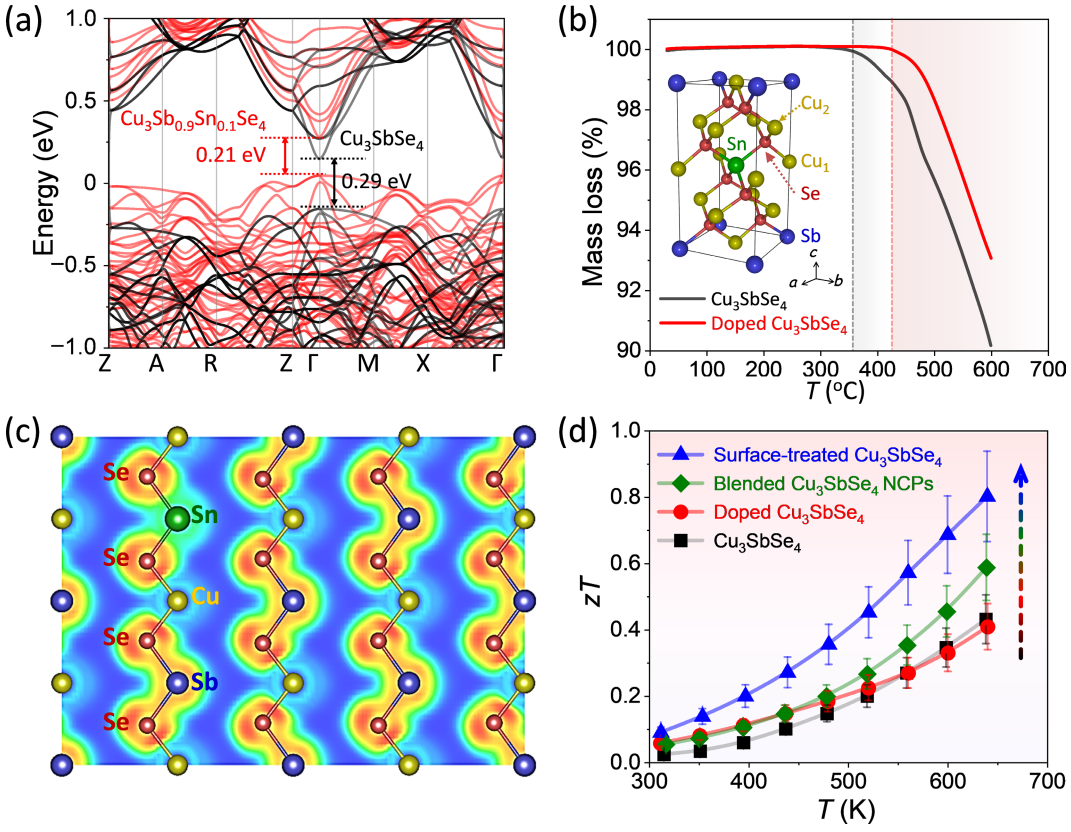

Figure 1 (a) Calculated band structure of Cu_3SbSe_4 and Sn-doped Cu_3SbSe_4. (b) TGA profile of annealed Cu_3SbSe_4 powder (black curve) and Sn-doped Cu_3SbSe_4 powder (red curve). The inset displays the unit cell of tetragonal Sn-doped Cu_3SbSe_4. (c) ELF of Sn-doped Cu_3SbSe_4 (110) surface. (d) Temperature-dependent zT values of Cu_3SbSe_4, doped Cu_3SbSe_4, surface-treated Cu_3SbSe_4, and blended Cu_3SbSe_4 NCPs.

surfactant-free SnSe NCs in anhydrous hexane. The solvent was then allowed to evaporate under a nitrogen atmosphere to ensure the stability and purity of the final product. The as-synthesized Cu_3SbSe_4 NCs were first thoroughly purified through multiple precipitation and re-dispersion steps, and then treated with NH_4SCN to efficiently remove any remaining OLA ligands from the matrix surface, obtaining ligand-free Cu_3SbSe_4 NCs [35]. Surfactant-free SnSe NCs were synthesized using a slightly modified version of a previously reported solution-processed method (Fig. S2 in the ESM) [49, 50].

The surface-treated Cu_3SbSe_4 NCs were obtained by magnetically stirring the as-produced Cu_3SbSe_4 NCs in an N-methyl formamide (MFA) solution containing SnSe molecular complexes for 48 h. The SnSe molecular complex solution was prepared by dissolving stoichiometric amounts of tin(II) oxide (SnO) and Se powder in a "thiol-amine" solution at room temperature under an inert atmosphere. At the temperature of 350–375 °C , this complex thermally crystallizes to yield a mixture of SnSe and $SnSe_2$ products [51]. Following this preparation, the surface-treated Cu_3SbSe_4 NCs were isolated from the solution, sequentially washed with acetone, and then dried under vacuum for 6 h at 60 °C to ensure the complete removal of impurities and solvents. Further details of these procedures can be found in the Experimental section in the ESM. It should be noted that, aside from the bare Cu_3SbSe_4 samples serving as the matrix, the amount of Sn was uniformly maintained at a 10% molar ratio in the other three samples.

Figure 2(a) displays a representative transmission electron microscopy (TEM) image of the synthesized spherical Cu_3SbSe_4 NCs, which exhibit uniformity in size with an average diameter of 16 ± 3 nm (Fig. S3 in the ESM). The doped Cu_3SbSe_4 NCs, shown in Fig. 2(b), display quasi-spherical morphologies with an average size of 18 ± 3 nm, and a broader distribution in both size and shape, consistent with findings from our previous report [35, 41]. Figure 2(c) displays a TEM image of Cu_3SbSe_4 NCs functionalized with SnSe molecular complexes, exhibiting slight variations in morphology due to the surface treatment processes (Fig. S4 in the ESM). It is also evident that the presence of OLA ligands on the surface of the Cu_3SbSe_4 NCs contributes to the well-distributed appearance in the TEM images of both the Cu_3SbSe_4 and doped Cu_3SbSe_4 samples (Figs. 2(a) and 2(b)) [35]. In contrast, the blended Cu_3SbSe_4 NCPs and the surface-treated Cu_3SbSe_4 samples exhibit aggregation, resulting from the removal of the original surface organic ligands or their replacement with shorter organic chain molecular complexes (Figs. 2(c) and 2(d), and Fig. S5 in the ESM) [52]. Figure 2(e) presents the electron energy loss spectroscopy (EELS) analysis of a single surface-treated Cu_3SbSe_4 NC, revealing the presence and uniform distribution of Cu, Sb, and Se atoms throughout the particle, as well as highlighting the presence of Sn atoms on the surface of the NC. The X-ray diffraction (XRD) patterns reveal that among the four samples analyzed with the measurement angle ranging from 20° to 80°, only the blended Cu_3SbSe_4 NCPs exhibit minor peaks, consistent with the orthorhombic phase of SnSe (PDF 00-048-1224), while the other three samples show no evidence of secondary phases within the detection limits of the XRD measurement (Fig. 2(f)).

All samples underwent a sequential process of ligand displacement and annealing to mitigate the influence of organic ligands on the electrical transport properties of the densified bulk

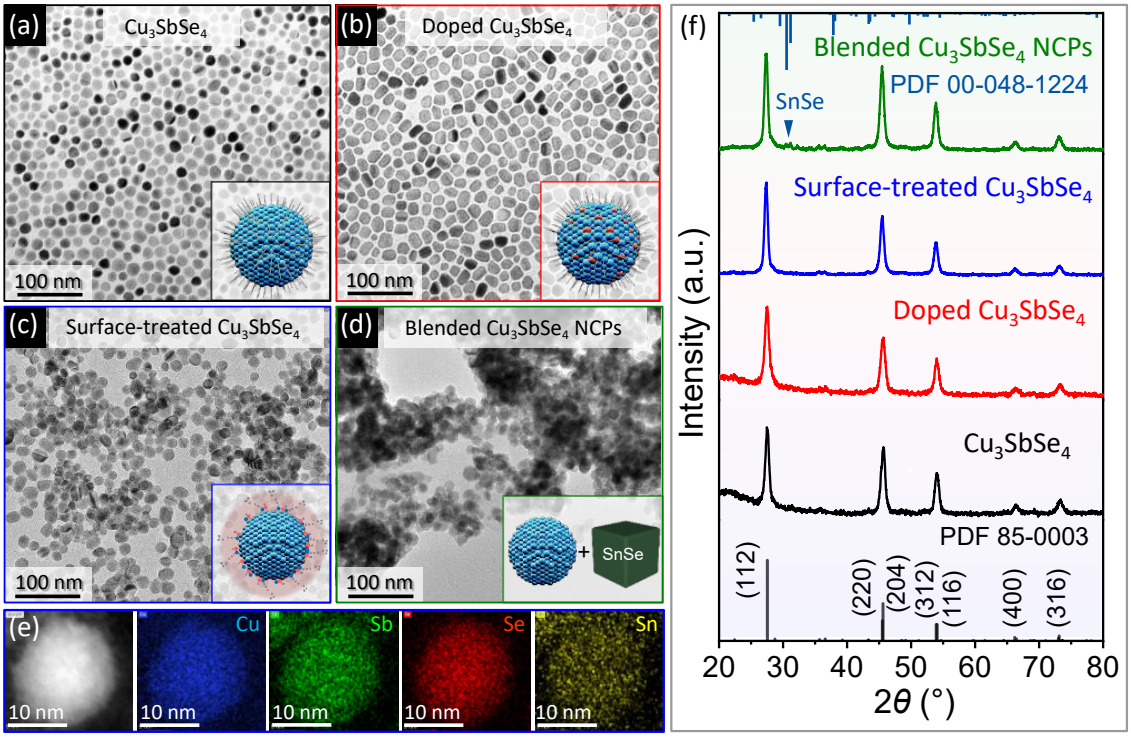

Figure 2 Representative TEM micrographs of (a) the Cu_3SbSe_4 NCs, (b) doped Cu_3SbSe_4 NCs, (c) surface-treated Cu_3SbSe_4 NCs, and (d) blended Cu_3SbSe_4 NCPs. The insets show schematic diagrams of the corresponding nanoparticles. (e) Annular dark field STEM (ADF-STEM) image of a single surface-treated Cu_3SbSe_4 NC and areal density of each of the elements extracted from the EELS spectrum image. (f) XRD patterns of the Cu_3SbSe_4 NCs, doped Cu_3SbSe_4 NCs, surface-treated Cu_3SbSe_4 NCs, and blended Cu_3SbSe_4 NCPs, including the PDF 85-0003 reference of Cu_3SbSe_4 (black vertical lines).

pellets and to ensure their thermal stability, as detailed in the Experimental section in the ESM. Subsequently, to assess the TE performance, the annealed nanopowders were hot-pressed by applying an uniaxial pressure of 60 MPa at 380 °C for 15 min, forming bulk pellets (Ø10 mm × 1.5 mm in height). This process yielded pellets with densities exceeding 92% of the theoretical value (Table S1 in the ESM) and demonstrated robust mechanical properties. XRD patterns (Fig. S6 in the ESM) reveal that all samples, except for the surface-treated Cu_3SbSe_4 pellet, exhibit weak secondary phases of Sb_2Se_3, while the surface-treated Cu_3SbSe_4 and blended Cu_3SbSe_4 NCPs samples additionally displayed minor peaks of SnO_2, which will most probably influence their electrical and thermal transport properties as discussed below.

The compositions of the consolidated bare Cu_3SbSe_4, doped Cu_3SbSe_4, surface-treated Cu_3SbSe_4, and blended Cu_3SbSe_4 NCPs pellets, as determined by energy-dispersive X-ray (EDX) spectroscopy analysis, matched their nominal values, within experimental error (Table S2 in the ESM). Notably, the corresponding EDX elemental mapping for the pellets shows a relatively homogeneous distribution of these elements, with no detectable Sb_2Se_3 precipitates, as shown in Figs. S7–S9 in the ESM.

2.2 Pellets microstructure

Figures 3(a)–3(h) display the scanning electron microscopy (SEM) images of the annealed powders and fractured pellets. SEM characterization indicates that upon the annealing and consolidation, the NCs within all samples experienced additional growth, resulting in the formation of grains ranging in size from tens to several hundred nanometers. This is attributed to the annealing mechanisms and the thermodynamic properties inherent to the materials. Notably, compared to Cu_3SbSe_4, the doped Cu_3SbSe_4, surface-treated Cu_3SbSe_4, and blended Cu_3SbSe_4 NCPs exhibit distinct microstructures.

In particular, cross-section SEM characterization of the doped Cu_3SbSe_4 sample displays smaller grain sizes and an abundance of nanoscale grains (Fig. 3(f)), attributed to the incorporation of Sn into the Sb sites within the Cu_3SbSe_4 lattice during the synthesis process (Fig. 3(i)). As noted above, this substitution directly strengthens the Sn–Se and neighboring Cu–Se bonds, thereby establishing a more stable chemical framework. This is evidenced by the calculated electron localization function (ELF) (Fig. 1(c)), which prevents the agglomeration of particles into larger grains, thereby enhancing the thermal stability of the samples (Fig. 1(b)).

The blended Cu_3SbSe_4 NCPs pellet exhibits smaller grain sizes but it operates through a different mechanism compared to the doped Cu_3SbSe_4 sample. The limited growth of the blended Cu_3SbSe_4 NCPs is attributed to the Zener pinning effect [53, 54], where the presence of SnSe as a secondary phase at the grain boundaries of the NCPs significantly reduces the driving force for grain boundary migration, thereby inhibiting grain growth (Fig. 3(k)). This phenomenon is similar to that observed in previously reported systems such as SnSe-CdSe [55, 56], SnSe-PbSe [57], and SnTe-Bi_2S_3 [58], despite differing sample processing methods.

In the samples obtained through surface treatment of the Cu_3SbSe_4 NCs with SnSe molecular complexes, only slight changes in shape and size were observed following the thiol-amine surface treatment (Fig. S4 in the ESM). After the annealing and consolidation steps, the particles underwent significant coalescence and growth into larger crystallographic domains, with sizes ranging from several hundred nanometers to ca. 1 μm, as shown in Figs. 3(c) and 3(g). This phenomenon is attributed to grain growth by

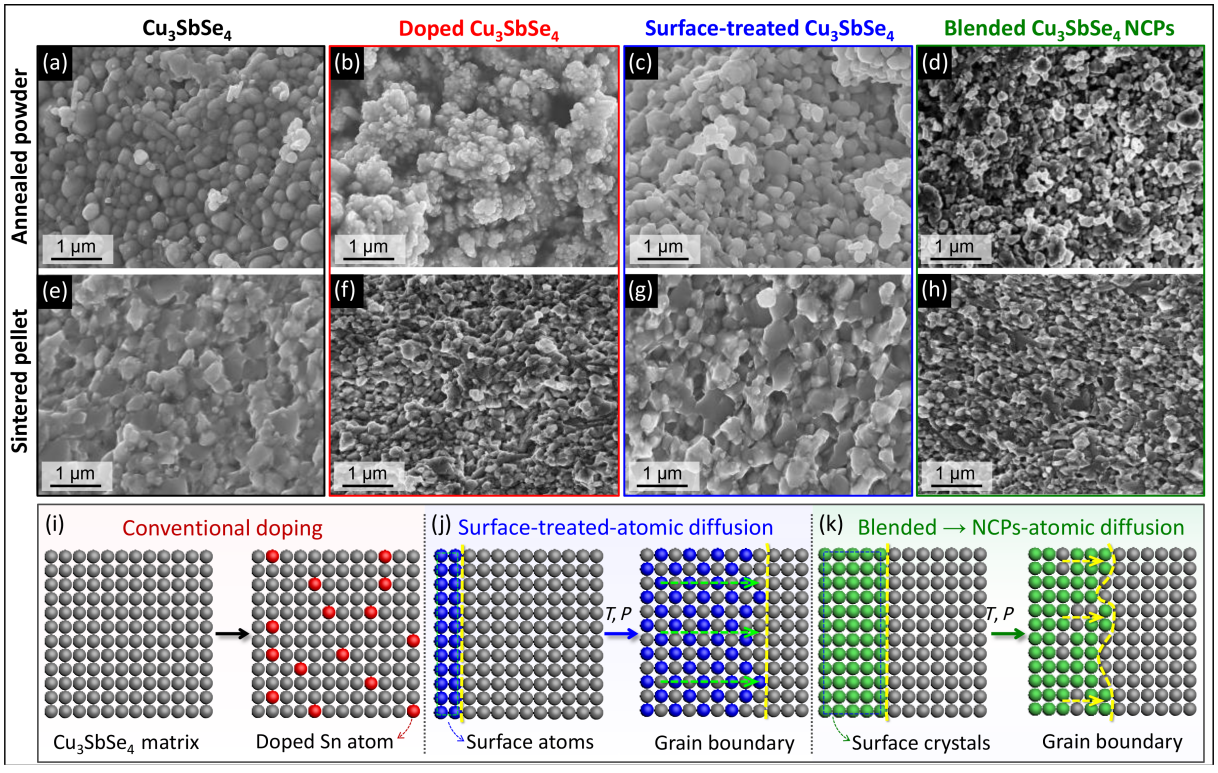

Figure 3 Representative SEM images of (a)–(d) annealed powders and (e)–(h) the fractured surfaces of pellets obtained from Cu_3SbSe_4, doped Cu_3SbSe_4, surface-treated Cu_3SbSe_4, and blended Cu_3SbSe_4 NCPs, respectively. (i) A scheme of extrinsic dopants during synthesis. Schematics of diffusion-induced grain boundary migration: (j) surface-treatment and (k) blending process.

diffusion-induced boundary movement during the pressure-assisted sintering in the hot press process. In this process, the high temperatures and pressures aided the migration of Cu_3SbSe_4 from the surface to inside the grain, driving the grain boundaries to migrate along atomic diffusion paths. This migration enabled the integration of the surface SnSe molecular complexes into the grain interior, forming a solid solution, as shown in Fig. 3(j). Faster atomic diffusion within the formed solid solution accelerated the grain growth in the surface-treated Cu_3SbSe_4 [59, 60]. EDX mapping in Fig. S8 in the ESM confirms the uniform distribution of Sn within the Cu_3SbSe_4 matrix after the annealing and consolidation processes, substantiating the inward atomic diffusion process. As discussed below, the increased grain sizes and related reduction of the density of grain boundaries diminished electron scattering at these boundaries, leading to enhanced carrier mobility in the surface-treated Cu_3SbSe_4.

To further evaluate the microstructure of the consolidated surface-treated Cu_3SbSe_4 material, TEM characterization was performed (Fig. 4 and Fig. S10 in the ESM). Figure 4(a) displays a dark-field scanning TEM (STEM) image of surface-treated Cu_3SbSe_4 pellet lamella obtained using the focused ion beam, displaying a heterogeneous grain size distribution ranging up to several hundred nanometers. Figures 4(b_1)–4(b_4) present corresponding EDX elemental maps, which reveal regions enriched with Sb and deficient in Cu. The diffraction pattern from an individual grain, highlighted by a yellow square in Fig. 4(a), reveals that the grains are single crystal domains with a body-centered tetragonal Cu_3SbSe_4 phase (space group: $I\bar{4}2m$), as shown in Fig. 4(c). Additionally, this pattern reveals ordered structures within the grain, as evidenced by the extra diffraction spots marked with yellow arrows in Fig. 4(c_1), indicating cation ordering.

Figure 4(d) displays a high-resolution TEM (HRTEM) of a grain's internal structure, revealing a highly defective grain with perfect atomic arrangements only over short lengths of approximately 5 nm. This HRTEM image corresponds with the general TEM micrograph shown in Fig. 4(c), which illustrates the grain structure as being significantly defective. The corresponding fast Fourier transform (FFT), the inset in this image, confirms the selected area diffraction (SAED) pattern previously presented and further verifies the presence of ordered structures within the Cu_3SbSe_4 matrix, while this specific grain, composed of the tetragonal Cu_3SbSe_4 phase, is visualized along its [111] zone axis. The main diffraction spots of the Cu_3SbSe_4 phase, highlighted with yellow circles, coincide with their inverse FFT (Fig. 4(e)). This inverse FFT image clearly reveals the prevalence of defects within the structure of the matrix phase. Additionally, the other diffraction spots, not encircled in yellow and generated by ordered structures within the matrix, are illustrated through their inverse FFT in green in Fig. 4(f). This image demonstrates that such ordered structures, i.e., cation ordering, match the periodic structure of the matrix phase in scale. The FFT further reveals that all fundamental diffraction spots arise from the coalescence of multiple diffraction spots rather than from a single sharp spot, consistent with the defected structure of the matrix phase, potentially due to compositional fluctuations within the matrix.

The dilatation map of this HRTEM image, including rotation (±10° rotation, Fig. S10(d) in the ESM) and dilatation (±10% strain range, Fig. 4(g)) geometric phase analysis (GPA) maps, derived using a Gaussian type of mask around the $\boldsymbol{g} = (4\bar{4}0)$ spot in the FFT, effectively demonstrates the distribution of normal strain components ε_{xx}, ε_{yy}, and ε_{xy} within this strain range, as shown in

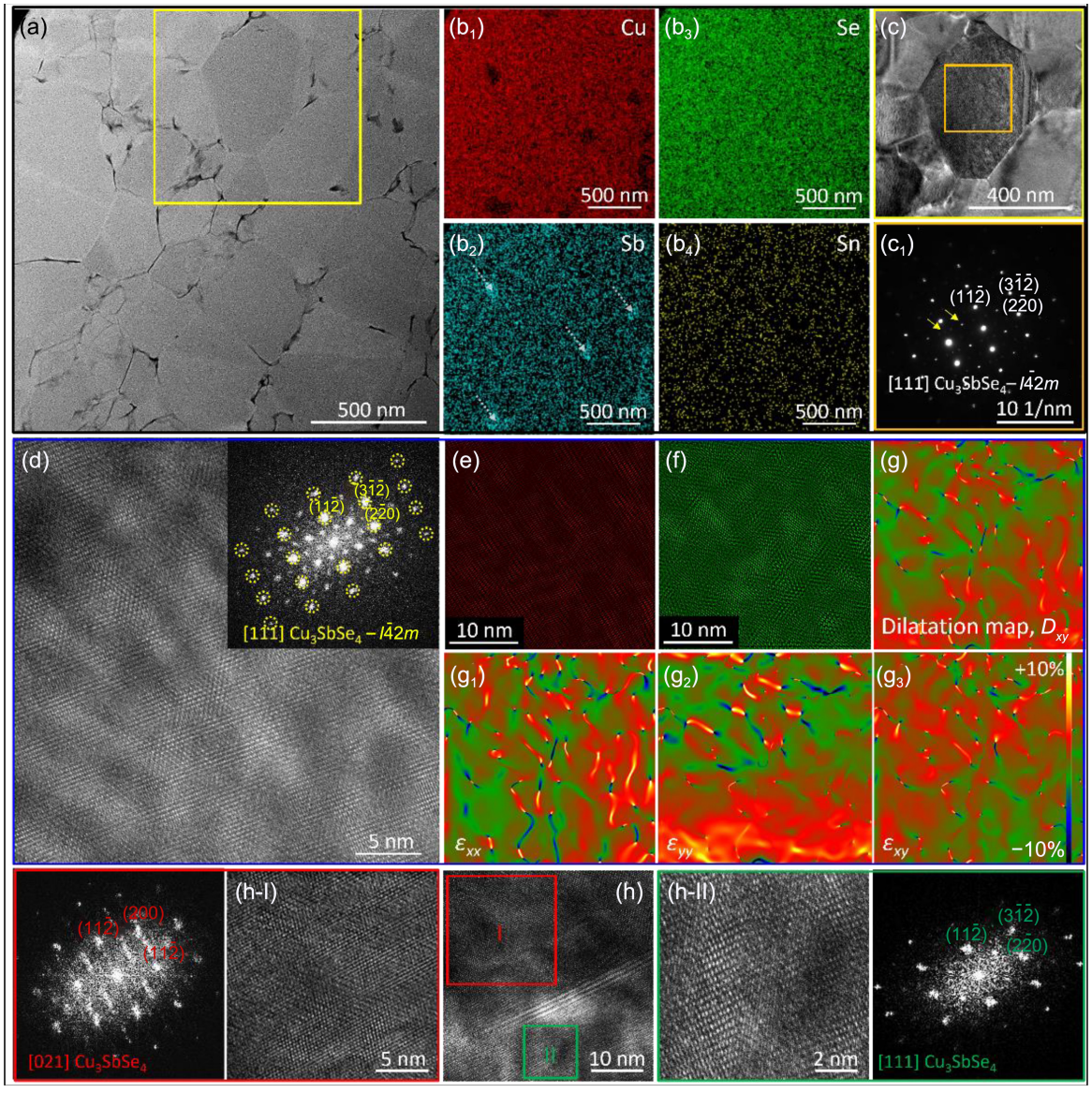

Figure 4 (a) General dark-field STEM image of the surface-treated Cu_3SbSe_4 pellet lamella, displaying a heterogeneous grain size distribution. (b) Corresponding EDX elemental maps for (b_1) Cu, (b_2) Sb, (b_3) Se, and (b_4) Sn. (c) TEM image taken from the yellow-squared region in (a), and (c_1) the SAED pattern obtained from the individual grain in the framed region in (c). (d) HRTEM image taken from an individual grain, with the inset being FFT pattern of this HRTEM image. (e) Inverse FFT of the yellow-circled main set of diffraction spots in the inset of (d). (f) Inverse FFT of the additional set of diffraction spots generated by the ordered structures. (g) Dilatation (±10% strain range) GPA maps obtained from the FFT of the HRTEM image, showing the distribution of the normal strain components (g_1) ε_{xx}, (g_2) ε_{yy}, and (g_3) ε_{xy} within the ±10% strain range obtained by GPA. (h) HRTEM image of a grain boundary: (h-I) the enlarged view of the red-squared area with the corresponding FFT along the [021] zone axis, and (h-II) the enlarged region of the green-squared area with the corresponding FFT, along the [111] zone axis.

Figs. 4(g_1)–4(g_3). The rotation and dilatation maps reveal numerous strain fields within the grain, consistent with the generally defective structure of the matrix phase.

Figure 4(h) presents the HRTEM image of a grain boundary where defects are clearly visible along the boundary. The FFT of the region highlighted in red confirms that the grain consists of the tetragonal Cu_3SbSe_4 phase visualized along its [021] zone axis (Fig. 4(h-I)), while the FFT of the region marked in green shows that this grain is also composed of the tetragonal Cu_3SbSe_4 phase but visualized along its [111] zone axis (Fig. 4(h-II)). Consequently, following the annealing and consolidation processes, the microstructure of the Cu_3SbSe_4 matrix treated with SnSe molecular complexes exhibited no secondary SnSe phase. This observation further confirms the high doping efficiency of Sn within the matrix, despite the thermal treatment temperatures being significantly lower than those employed in the traditional solid-state method to produce Sn-doped systems.

2.3 Electronic transport properties

Figure 5 shows the electronic transport properties of the four Cu_3SbSe_4-based samples as a function of temperature, ranging from approximately 310 to 640 K, including Cu_3SbSe_4, doped Cu_3SbSe_4, surface-treated Cu_3SbSe_4, and blended Cu_3SbSe_4 NCPs. The pristine Cu_3SbSe_4 sample exhibits a low σ of approximately 7.8 S·cm^{-1} at room temperature, increasing to 29.4 S·cm^{-1} at 640 K (Fig. 5(a)). This increase in σ with temperature suggests that thermal excitation of charge carriers plays an important role in controlling the σ in this material, indicating an intrinsic or moderately doped

semiconductor behavior consistent with previous studies [34, 35, 41]. Notably, the σ values of the doped Cu_3SbSe_4, surface-treated Cu_3SbSe_4, and blended Cu_3SbSe_4 NCPs samples are consistently higher and all exhibit degenerate semiconductor behavior, characterized by a decrease in σ with increasing temperature. In particular, the doped Cu_3SbSe_4 sample exhibits an exceptional σ of 770 S·cm^{-1} at room temperature, two orders of magnitude higher than that of bare Cu_3SbSe_4. The surface-treated Cu_3SbSe_4 and blended Cu_3SbSe_4 NCPs samples exhibit relatively lower σ across the entire temperature range, which is attributed to the presence of trace amounts of high-resistivity tin oxide, as evidenced by XRD characterization (Fig. S6 in the ESM). As part of the surface SnSe readily forms a layer of SnO_x, Sn's capacity to contribute as acceptor dopant by Sb substitution is diminished [61, 62].

All four pellets exhibit an intrinsic p-type semiconductor character, consistently displaying positive Seebeck coefficient (S) values across the entire temperature range (Fig. 5(b)). Very high S values were obtained in bare Cu_3SbSe_4, attributed to the low Hall charge carrier concentration (p_H) in this material and the intricate electronic structure inherent to Cu_3SbSe_4, characterized by multiple energy bands, as detailed by the density functional theory (DFT) calculations in Fig. 1(a). The S values of bare Cu_3SbSe_4 exhibit an initial increase, followed by a slight decrease as the temperature rises, consistent with previous report [34, 35, 41, 42]. Conversely, all the samples containing Sn exhibit much lower S (Fig. 5(b)), which is associated to their higher p_H.

Room temperature Hall measurements were conducted to determine the p_H and carrier mobility (μ_H). Figure 5(c) shows that the p_H for undoped Cu_3SbSe_4 is only 3.2 × 10^{18} cm^{-3}. With the addition of 10% Sn, a two order of magnitude increase in p_H, to ca. 2.5 × 10^{20} cm^{-3}, is obtained for the doped Cu_3SbSe_4, thereby demonstrating Sn as a highly effective dopant in this system. DFT calculations were used to examine the impact of Sn doping on the band structure of Cu_3SbSe_4 (Fig. 1(a) and Fig. S11 in the ESM). The computed band gaps (E_g) were ca. 0.29 eV for bare Cu_3SbSe_4 and 0.21 eV for Sn-doped Cu_3SbSe_4. This reduction in the band gap, consistent with previous first-principles studies [37, 38], demonstrates the shift of the Fermi level from the bandgap region into the valence band, correlating with an increase in p_H and aligning with the experimental measurements presented (Fig. 5(c)). Interestingly, the blended Cu_3SbSe_4 NCPs sample exhibits a higher p_H compared to the surface-treated Cu_3SbSe_4, which could be attributed to the incorporation of SnSe NCs within the Cu_3SbSe_4 matrix, providing a larger number of Sn^{2+} ions capable of supplying more holes than those in the surface-treated Cu_3SbSe_4. Moreover, the susceptibility of the SnSe molecular complexes used for surface treatment to oxidize into the higher valence state of Sn^{4+} significantly reduces the ability of Sn^{2+} as an acceptor dopant in TE materials, further confirmed by X-ray photoelectron spectroscopy (XPS) characterization (Fig. S12 in the ESM). This phenomenon is also consistent with previous studies [63].

Compared with bare Cu_3SbSe_4, the doped Cu_3SbSe_4 exhibits relatively lower μ_H, which can be attributed to two main factors. (i) The doped Cu_3SbSe_4 possesses significantly smaller grain sizes, resulting in increased charge carrier scattering at grain boundaries. (ii) The decrease in μ_H is associated with an increase in the density of state (DOS) by DFT calculations (Fig. S11 in the ESM) and m_d^* by the single parabolic band (SPB) model. Among all these samples, the surface-treated Cu_3SbSe_4 exhibits the highest μ_H, attributable to the largest grain size, which facilitates charge carrier transport within the bulk. Consequently, even though the blended Cu_3SbSe_4 has a higher p_H, it exhibits identical σ to that of the surface-treated

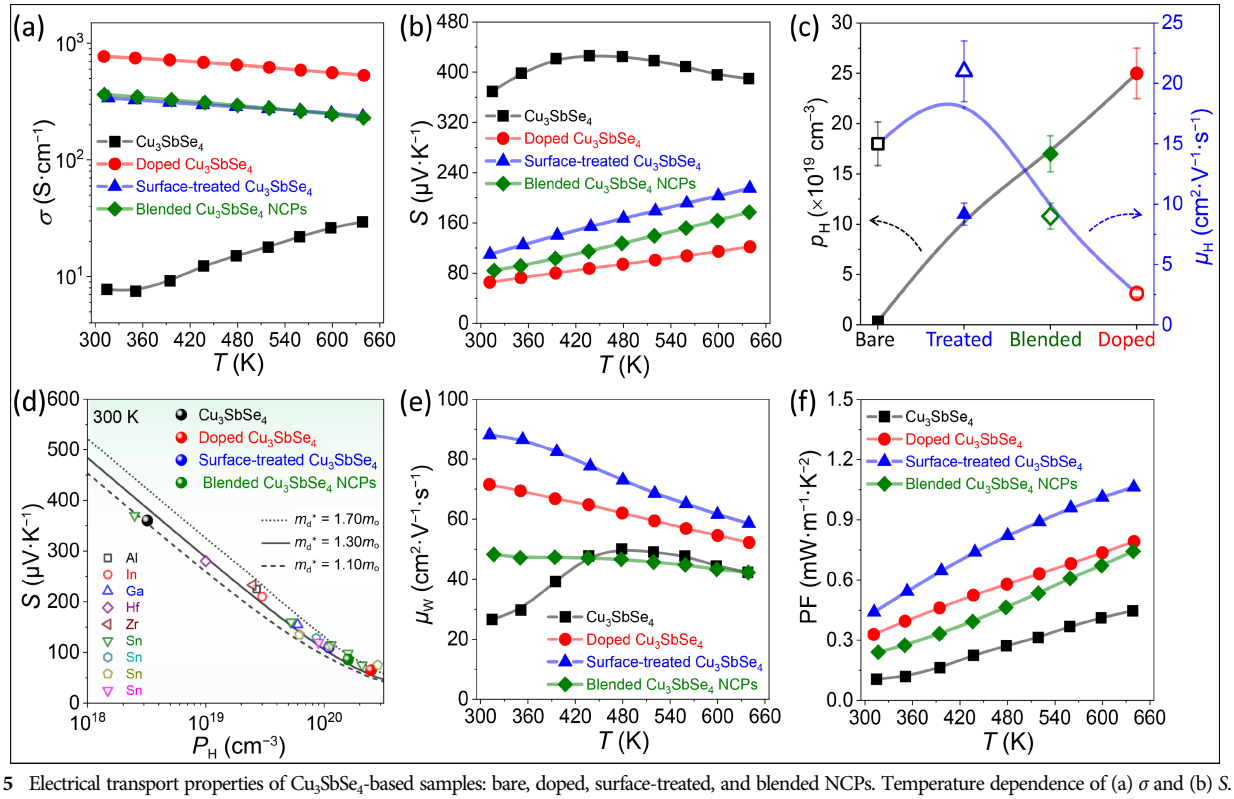

Figure 5 Electrical transport properties of Cu_3SbSe_4-based samples: bare, doped, surface-treated, and blended NCPs. Temperature dependence of (a) σ and (b) S. (c) p_H and μ_H at room temperature. (d) Pisarenko plot at 300 K with open dots representing reported Cu_3SbSe_4-based systems [34, 35, 40, 44, 66, 68]. Temperature dependence of (e) μ_W and (f) PF.

Cu_3SbSe_4. The Pisarenko plot at 300 K, with S as the vertical coordinate and p_H as the horizontal coordinate, confirms a slight increase in the m_d^* value for Cu_3SbSe_4 upon Sn introduction (Fig. 5(d)). This finding is consistent with electronic structure calculations (Fig. 1(a) and Fig. S11 in the ESM) and previous studies [34, 44, 45].

Using the S and σ values, which provide a p_H-independent mobility parameter reflecting the average mobility across all conductive channels, we calculated the weighted mobilities (μ_W) for all samples [64], revealing that the surface-treated Cu_3SbSe_4, which exhibits the highest μ_W, demonstrates superior electrical transport properties (Fig. 5(e)). This calculation facilitates the optimization of PF by balancing σ and S, which is essential for enhancing TE efficiency and understanding the influence of microstructural features on electrical transport properties. Subsequently, σ and S values were utilized to calculate the PFs, as shown in Fig. 5(f), where the PFs of the doped Cu_3SbSe_4, surface-treated Cu_3SbSe_4, and blended Cu_3SbSe_4 NCPs samples are significantly higher than that of bare Cu_3SbSe_4. Notably, the surface-treated Cu_3SbSe_4 achieves the maximum PF values across the entire temperature range, reaching 1.1 $mW \cdot m^{-1} \cdot K^{-2}$ at 640 K, which is significantly larger than that of pristine Cu_3SbSe_4 and exceeds previously reported values for Cu_3SbSe_4-based compounds [41, 42, 45, 65–67].

2.4 Thermal transport properties

The κ_{tot} values of all the pellets consistently decrease with temperature throughout the whole temperature range, yielding relatively low values, as shown in Fig. 6(a). In pristine Cu_3SbSe_4, the κ_{tot} value drops to 0.66 $W \cdot m^{-1} \cdot K^{-1}$ at 640 K, which is lower than those reported for bulk Cu_3SbSe_4 materials produced through solid-state methods [34, 43–45, 67, 69–72]. The lattice thermal conductivity (κ_L) values were calculated using the equation $\kappa_L = \kappa - \kappa_e$, with $\kappa_e = L_o \sigma T$, following the Wiedemann–Franz law [73], where L_o is the Lorenz number (Fig. S13(a) in the ESM) calculated based on the measured S values [74]. In contrast, the other three samples exhibit higher κ_{tot} values compared to bare Cu_3SbSe_4, primarily due to the increased κ_e contributions (Fig. S13(c) in the ESM). All samples, including bare Cu_3SbSe_4, exhibit extremely low κ_L, with the doped Cu_3SbSe_4, surface-treated Cu_3SbSe_4, and blended Cu_3SbSe_4 NCPs samples displaying slightly lower κ_L values than the bare Cu_3SbSe_4 (Fig. 6(b)). The surface-treated Cu_3SbSe_4 sample, even with the larger grain size, maintains a relatively low κ_L, which is attributed to its highly defective structure, regions with higher Sb content, and numerous lattice strains within the grains (Fig. 4).

These κ_L values are significantly lower than those typically reported for most Cu_3SbSe_4-based materials prepared via solid-state and/or solution-processing methods, as shown in Fig. 6(c) [34, 39, 40–44, 47, 48, 65, 70, 71], and approach the theoretical limit for the amorphous state, estimated at ca. 0.47 $W \cdot m^{-1} \cdot K^{-1}$ according to the Cahill's model [34, 75, 76]. To further understand the low κ_L, we analyzed the phonon dispersion relations of Cu_3SbSe_4 (Fig. 6(d)) and the partial phonon density of states (PDOS, Fig. 6(e)) to explore the underlying causes of its low κ_L. Low and high frequency modes are predominantly influenced by Cu, Sb, and Se atoms, respectively. In Fig. 6(f), we illustrated the relationship between phonon group velocity (v) and frequency (ω), where the group velocity aligns with those of typical TE materials possessing inherently low κ_L. These analyses reveal that intrinsic Cu_3SbSe_4

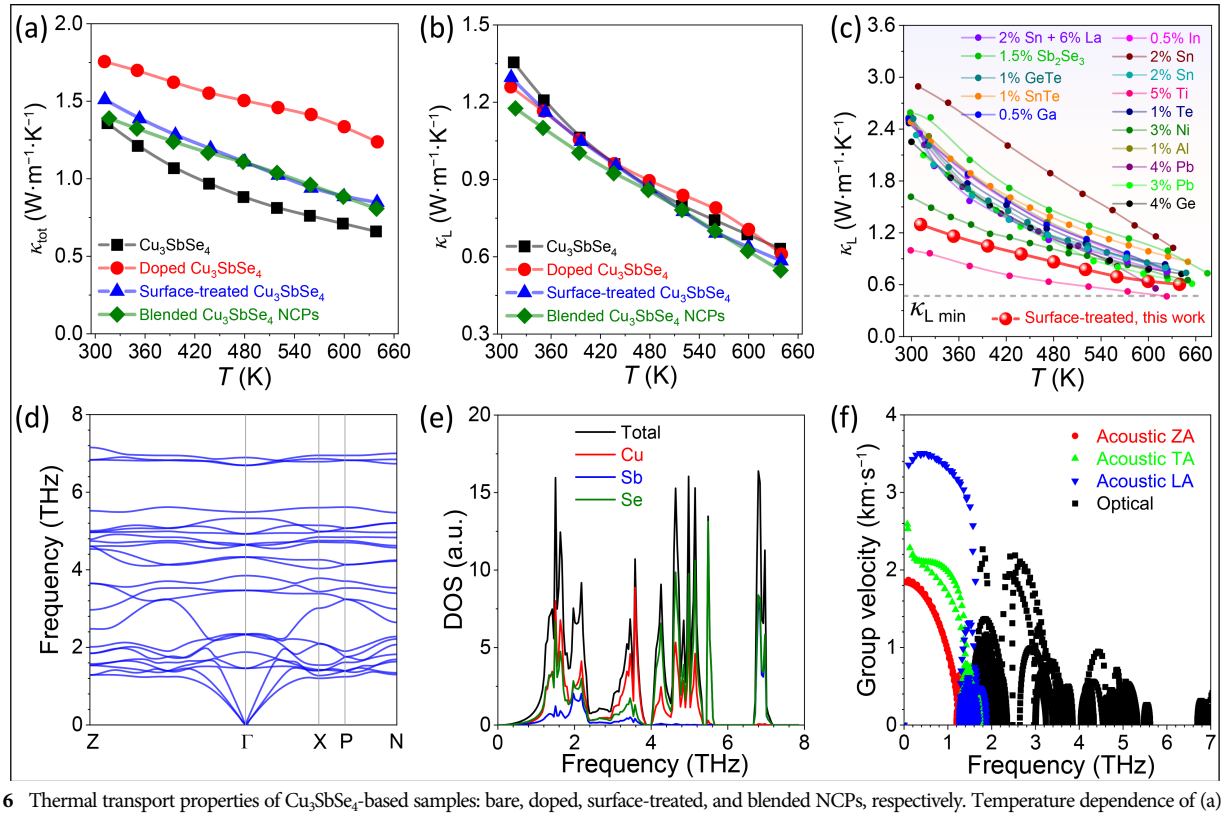

Figure 6 Thermal transport properties of Cu_3SbSe_4-based samples: bare, doped, surface-treated, and blended NCPs, respectively. Temperature dependence of (a) κ_{tot} and (b) κ_L. (c) Comparison of κ_L for reported state-of-the-art Cu_3SbSe_4-based materials, including 2% SnTe [70], 1% GeTe [48], 1.5% Bi_2Se_3 [71], 2% Sn + 6% La [44], 4% Ge [39], 0.5% Ga [40], 0.5% In [40], 1% Al [40], 3% Ni [43], 3% Pb [41], 4% Pb [65], 2% Sn [34,44], 5% Ti [42], and 1% Te [47]. The results obtained in the present work are indicated with solid red dots and lines. (d) Phonon dispersion, (e) PDOS, and (f) phonon group velocity of Cu_3SbSe_4 at 300 K.

exhibits robust coupling within the acoustic branches and between the acoustic and low-frequency optical branches, significantly contributing to its inherently low κ_L. Additionally, previous studies have shown that introducing Sn into the Cu_3SbSe_4 matrix minimally impacts low-frequency phonons, thereby ensuring the sample maintains low κ_L [45].

Overall, the simultaneous improvement in electrical and thermal transport properties enables achieving a zT_{max} value of 0.80 at 640 K for the surface-treated Cu_3SbSe_4 sample (Fig. 1(d)), which is ca. 1.9 times that of bare Cu_3SbSe_4 in the present work and is comparable to some of notable values obtained from doped Cu_3SbSe_4 and Cu_3SbSe_4-based composites prepared via solid-state or solution-processing methods (Fig. S13(d) in the ESM). Importantly, the results obtained from both the doped and surface-treated Cu_3SbSe_4 samples exhibit remarkable stability, consistently maintaining performance during cycling tests (Fig. S14 in the ESM). Compared to the conventional doping and the simple blending methods for constructing NCPs, the surface-treatment strategy using molecular complexes offers significant advantages for synergistically optimizing carrier and phonon transport. By functionalizing the high-energy surface atoms of the matrix, this approach enables the construction of desired materials through a simplified post-processing procedure, particularly crucial for material systems requiring precise grain refinement or those aiming to promote grain growth. Additionally, the surface treatment method holds potential for large-scale production using techniques such as spray coating or dip coating; however, challenges such as achieving uniform treatment and ensuring the stability of the molecular complexes during production remain for industrial implementation.

3 Conclusions

In this work, a scalable and high yield approach to synthesizing Cu_3SbSe_4 NCs was studied in detail. These NCs were further used for the production of Cu_3SbSe_4 nanomaterials that were doped with Sn using three distinct strategies: conventional atomic doping during the NC synthesis step, surface treatment of the NC building blocks with SnSe molecular complexes, and blending of Cu_3SbSe_4 with SnSe NCs to form NCPs. The thorough analysis of the structural characteristics and charge and thermal transport properties of the materials obtained after annealing and hot pressing the NC building blocks under identical conditions provided a comprehensive understanding of the impact of Sn on the electrical and thermal transport mechanisms of Cu_3SbSe_4. Both computational and experimental results revealed that surface treatment using SnSe molecular complexes significantly enhances the TE performance of Cu_3SbSe_4 compared to conventional doping and blending methods. The surface-treated Cu_3SbSe_4 sample achieved the highest PF and a maximum zT value of 0.80 at 640 K, demonstrating promising performance among high-performing doped Cu_3SbSe_4-based materials and composites prepared via solid-state and solution-processing methods. This study underscores the significant advantages of using surface molecular complexes in optimizing charge and thermal transport properties in nanomaterials produced from the bottom-up assembly of NC building blocks, presenting a promising strategy for development of next generations of functional nanomaterials, including for TE and other applications.

Electronic Supplementary Material: Supplementary material (details of the chemicals used, NC synthesis, pellet fabrication, additional materials characterization (XRD patterns, SEM, TEM, XPS patterns, and extra electrical and thermal characterization), material stability, pellet density and composition, and comparison with literature values) is available in the online version of this article at https://doi.org/10.26599/NR.2025.94907072.

Data availability

All data needed to support the conclusions in the paper are presented in the manuscript and the Electronic Supplementary Material. Additional data related to this paper may be requested from the corresponding author upon request.

Acknowledgements

Y. L. acknowledges funding from the National Natural Science Foundation of China (No. 22209034), the Innovation and Entrepreneurship Project of Overseas Returnees in Anhui Province (No. 2022LCX002), and the Fundamental Research Funds for the Central Universities (No. JZ2024HGTB0239). K. H. L. acknowledges financial support from the National Natural Science Foundation of China (No. 22208293). M. I. acknowledge financial support from ISTA and the Werner Siemens Foundation. M. H. acknowledges funding from Australian Research Council (No. FT230100316). L. L. H. and S. H. W. acknowledge the Fundamental Research Funds for the Central Universities (Nos. JZ2023HGTA0179 and JZ2024HGTA0170).

Declaration of competing interest

All the contributing authors report no conflict of interests in this work.

Author contribution statement

S. S. X.: Data curation, investigation, writing – original draft, experimental design. M. J. Z.: Data curation, software, formal analysis. M. Q. L.: Data curation, software, validation. S. H. W.: Software, formal analysis. A. G.: Software, formal analysis. L. L. H.: Formal analysis. L. C.: Software. Y. Z.: Formal analysis, writing – review & editing. M. I.: Formal analysis, writing – review & editing. K. H. L.: Project administration, funding acquisition, writing – review & editing. M. H.: Project administration, funding acquisition, writing – review & editing. Y. L.: Project administration, supervision, funding acquisition, writing – review & editing. A. C.: Project administration, writing – review & editing. All the authors have approved the final manuscript.

Use of AI statement

None.

References

[1] Bell, L. E. Cooling, heating, generating power, and recovering waste heat with thermoelectric systems. *Science* **2008**, *321*, 1457–1461.

[2] He, J.; Tritt, T. M. Advances in thermoelectric materials research: Looking back and moving forward. *Science* **2017**, *357*, eaak9997.

[3] Shi, X. L.; Zou, J.; Chen, Z. G. Advanced thermoelectric design: From

materials and structures to devices. *Chem. Rev.* **2020**, *120*, 7399–7515.
[4] Ortega, S.; Ibáñez, M.; Liu, Y.; Zhang, Y.; Kovalenko, M. V.; Cadavid, D.; Cabot, A. Bottom-up engineering of thermoelectric nanomaterials and devices from solution-processed nanoparticle building blocks. *Chem. Soc. Rev.* **2017**, *46*, 3510–3528.
[5] Liu, Y.; Ibáñez, M. Tidying up the mess. *Science* **2021**, *371*, 678–679.
[6] Tan, G. J.; Zhao, L. D.; Kanatzidis, M. G. Rationally designing high-performance bulk thermoelectric materials. *Chem. Rev.* **2016**, *116*, 12123–12149.
[7] Ibáñez, M.; Luo, Z. S.; Genç, A.; Piveteau, L.; Ortega, S.; Cadavid, D.; Dobrozhan, O.; Liu, Y.; Nachtegaal, M.; Zebarjadi, M. et al. High-performance thermoelectric nanocomposites from nanocrystal building blocks. *Nat. Commun.* **2016**, *7*, 10766.
[8] He, P. L.; Wu, Y. Constructing of highly porous thermoelectric structures with improved thermoelectric performance. *Nano Res.* **2021**, *14*, 3608–3615.
[9] Qin, Y. X.; Qin, B. C.; Hong, T.; Zhang, X.; Wang, D. Y.; Liu, D. R.; Wang, Z. Y.; Su, L. Z.; Wang, S. N.; Gao, X. et al. Grid-plainification enables medium-temperature PbSe thermoelectrics to cool better than Bi_2Te_3. *Science* **2024**, *383*, 1204–1209.
[10] Jiang, B. B.; Yu, Y.; Cui, J.; Liu, X. X.; Xie, L.; Liao, J. C.; Zhang, Q. H.; Huang, Y.; Ning, S. C.; Jia, B. H. et al. High-entropy-stabilized chalcogenides with high thermoelectric performance. *Science* **2021**, *371*, 830–834.
[11] Ibáñez, M.; Genç, A.; Hasler, R.; Liu, Y.; Dobrozhan, O.; Nazarenko, O.; de la Mata, M.; Arbiol, J.; Cabot, A.; Kovalenko, M. V. Tuning transport properties in thermoelectric nanocomposites through inorganic ligands and heterostructured building blocks. *ACS Nano* **2019**, *13*, 6572–6580.
[12] Cadavid, D.; Ortega, S.; Illera, S.; Liu, Y.; Ibáñez, M.; Shavel, A.; Zhang, Y.; Li, M. Y.; López, A. M.; Noriega, G. et al. Influence of the ligand stripping on the transport properties of nanoparticle-based PbSe nanomaterials. *ACS Appl. Energy Mater.* **2020**, *3*, 2120–2129.
[13] Li, M. Y.; Zhao, X. K.; Wang, D. Y.; Han, X.; Yang, D. W.; Wu, B. T.; Song, H. Z.; Jia, M. C.; Liu, Y.; Arbiol, J. et al. Enhancing the thermoelectric and mechanical properties of p-type PbS through band convergence and microstructure regulation. *Nano Lett.* **2024**, *24*, 8126–8133.
[14] Zhu, Z. Y.; Tiwari, J.; Feng, T. L.; Shi, Z.; Lou, Y.; Xu, B. High thermoelectric properties with low thermal conductivity due to the porous structure induced by the dendritic branching in n-type PbS. *Nano Res.* **2022**, *15*, 4739–4746.
[15] Zhu, T. J.; Liu, Y. T.; Fu, C. G.; Heremans, J. P.; Snyder, J. G.; Zhao, X. B. Compromise and synergy in high-efficiency thermoelectric materials. *Adv. Mater.* **2017**, *29*, 1605884.
[16] Hao, F.; Qiu, P. F.; Tang, Y. S.; Bai, S. Q.; Xing, T.; Chu, H. S.; Zhang, Q. H.; Lu, P.; Zhang, T. S.; Ren, D. D. et al. High efficiency Bi_2Te_3-based materials and devices for thermoelectric power generation between 100 and 300 °C. *Energy Environ. Sci.* **2016**, *9*, 3120–3127.
[17] Liu, Y.; Zhang, Y.; Lim, K. H.; Ibáñez, M.; Ortega, S.; Li, M. Y.; David, J.; Martí-Sánchez, S.; Ng, K. M.; Arbiol, J. et al. High thermoelectric performance in crystallographically textured n-type $Bi_2Te_{3-x}Se_x$ produced from asymmetric colloidal nanocrystals. *ACS Nano* **2018**, *12*, 7174–7184.
[18] Liu, Y.; Zhang, Y.; Ortega, S.; Ibáñez, M.; Lim, K. H.; Grau-Carbonell, A.; Martí-Sánchez, S.; Ng, K. M.; Arbiol, J.; Kovalenko, M. V. et al. Crystallographically textured nanomaterials produced from the liquid phase sintering of $Bi_xSb_{2-x}Te_3$ nanocrystal building blocks. *Nano Lett.* **2018**, *18*, 2557–2563.
[19] Zhang, H.; Momand, J.; Levinsky, J.; Guo, Q. K.; Zhu, X. T.; ten Brink, G. H.; Blake, G. R.; Palasantzas, G.; Kooi, B. J. Nanostructure and thermal power of highly-textured and single-crystal-like Bi_2Te_3 thin films. *Nano Res.* **2022**, *15*, 2382–2390.
[20] Wei, T. R.; Qin, Y. T.; Deng, T. T.; Song, Q. F.; Jiang, B. B.; Liu, R. H.; Qiu, P. F.; Shi, X.; Chen, L. D. Copper chalcogenide thermoelectric materials. *Sci. China Mater.* **2019**, *62*, 8–24.
[21] Qiu, P. F.; Shi, X.; Chen, L. D. Cu-based thermoelectric materials. *Energy Storage Mater.* **2016**, *3*, 85–97.
[22] Lim, K. H.; Li, M. Q.; Zhang, Y.; Wu, Y.; Zhou, Q. M.; Wang, Q. Y.; Yang, X.; Liu, P. W.; Wang, W. J.; Wong, K. W. et al. Modulation doping of p-type $Cu_{12}Sb_4S_{13}$ toward improving thermoelectric performance. *J. Mater. Sci. Technol.* **2024**, *171*, 71–79.
[23] Liu, W. D.; Yang, L.; Chen, Z. G.; Zou, J. Promising and eco-friendly Cu_2X-based thermoelectric materials: Progress and applications. *Adv. Mater.* **2020**, *32*, 1905703.
[24] Liu, H. L.; Shi, X.; Xu, F. F.; Zhang, L. L.; Zhang, W. Q.; Chen, L. D.; Li, Q.; Uher, C.; Day, T.; Snyder, G. J. Copper ion liquid-like thermoelectrics. *Nat. Mater.* **2012**, *11*, 422–425.
[25] He, Y.; Day, T.; Zhang, T. S.; Liu, H. L.; Shi, X.; Chen, L. D.; Snyder, G. J. High thermoelectric performance in non-toxic earth-abundant copper sulfide. *Adv. Mater.* **2014**, *26*, 3974–3978.
[26] Zhang, Y.; Xing, C. C.; Liu, Y.; Spadaro, M. C.; Wang, X.; Li, M. Y.; Xiao, K.; Zhang, T.; Guardia, P.; Lim, K. H. et al. Doping-mediated stabilization of copper vacancies to promote thermoelectric properties of $Cu_{2-x}S$. *Nano Energy* **2021**, *85*, 105991.
[27] Li, M. Y.; Liu, Y.; Zhang, Y.; Han, X.; Zhang, T.; Zuo, Y.; Xie, C. Y.; Xiao, K.; Arbiol, J.; Llorca, J. et al. Effect of the annealing atmosphere on crystal phase and thermoelectric properties of copper sulfide. *ACS Nano* **2021**, *15*, 4967–4978.
[28] Xing, C. C.; Zhang, Y.; Xiao, K.; Han, X.; Liu, Y.; Nan, B. F.; Ramon, M. G.; Lim, K. H.; Li, J. S.; Arbiol, J. et al. Thermoelectric performance of surface-engineered $Cu_{1.5-x}Te$-Cu_2Se nanocomposites. *ACS Nano* **2023**, *17*, 8442–8452.
[29] Ming, H. W.; Zhu, G. F.; Zhu, C.; Qin, X. Y.; Chen, T.; Zhang, J.; Li, D.; Xin, H. X.; Jabar, B. Boosting thermoelectric performance of Cu_2SnSe_3 via comprehensive band structure regulation and intensified phonon scattering by multidimensional defects. *ACS Nano* **2021**, *15*, 10532–10541.
[30] Song, J. M.; Liu, Y.; Niu, H. L.; Mao, C. J.; Cheng, L. J.; Zhang, S.-Y.; Shen, Y. H. Hot-injection synthesis and characterization of monodispersed ternary Cu_2SnSe_3 nanocrystals for thermoelectric applications. *J. Alloys Compd.* **2013**, *581*, 646–652.
[31] Huang, L. L.; Li, Y. Y.; Sha, S. M.; Ge, B. Z.; Wu, Y. C.; Yan, J.; Kong, Y.; Zhang, J. Engineering multiple microstructural defects for record-breaking thermoelectric properties of chalcopyrite $Cu_{1-x}Ag_xGaTe_2$. *Small* **2023**, *19*, 2206865.
[32] Plirdpring, T.; Kurosaki, K.; Kosuga, A.; Day, T.; Firdosy, S.; Ravi, V.; Snyder, G. J.; Harnwunggmoung, A.; Sugahara, T.; Ohishi, Y. et al. Chalcopyrite $CuGaTe_2$: A high-efficiency bulk thermoelectric material. *Adv. Mater.* **2012**, *24*, 3622–3626.
[33] Ibáñez, M.; Zamani, R.; LaLonde, A.; Cadavid, D.; Li, W. H.; Shavel, A.; Arbiol, J.; Morante, J. R.; Gorsse, S.; Snyder, G. J. et al. $Cu_2ZnGeSe_4$ nanocrystals: Synthesis and thermoelectric properties. *J. Am. Chem. Soc.* **2012**, *134*, 4060–4063.
[34] Wei, T. R.; Wang, H.; Gibbs, Z. M.; Wu, C. F.; Snyder, G. J.; Li, J. F. Thermoelectric properties of Sn-doped p-type Cu_3SbSe_4: A compound with large effective mass and small band gap. *J. Mater. Chem. A* **2014**, *2*, 13527–13533.
[35] Liu, Y.; García, G.; Ortega, S.; Cadavid, D.; Palacios, P.; Lu, J.; Ibáñez, M.; Xi, L.; De Roo, J.; López, A. M. et al. Solution-based synthesis and processing of Sn- and Bi-doped Cu_3SbSe_4 nanocrystals, nanomaterials and ring-shaped thermoelectric generators. *J. Mater. Chem. A* **2017**, *5*, 2592–2602.
[36] Berger, L. I.; Prochukhan, V. D. *Ternary diamond-like semiconductors*; Springer: New York, 2012.

[37] García, G.; Palacios, P.; Cabot, A.; Wahnón, P. Thermoelectric properties of doped-Cu_3SbSe_4 compounds: A first-principles insight. *Inorg. Chem.* **2018**, *57*, 7321–7333.

[38] Do, D. T.; Mahanti, S. D. Theoretical study of defects Cu_3SbSe_4: Search for optimum dopants for enhancing thermoelectric properties. *J. Alloys Compd.* **2015**, *625*, 346–354.

[39] Chang, C. H.; Chen, C. L.; Chiu, W. T.; Chen, Y. Y. Enhanced thermoelectric properties of Cu_3SbSe_4 by germanium doping. *Mater. Lett.* **2017**, *186*, 227–230.

[40] Zhang, D.; Yang, J. Y.; Jiang, Q. H.; Zhou, Z. W.; Li, X.; Xin, J. W.; Basit, A.; Ren, Y. Y.; He, X.; Chu, W. J. et al. Combination of carrier concentration regulation and high band degeneracy for enhanced thermoelectric performance of Cu_3SbSe_4. *ACS Appl. Mater. Interfaces* **2017**, *9*, 28558–28565.

[41] Wan, S. H.; Xiao, S. S.; Li, M. Q.; Wang, X.; Lim, K. H.; Hong, M.; Ibáñez, M.; Cabot, A.; Liu, Y. Band engineering through Pb-doping of nanocrystal building blocks to enhance thermoelectric performance in Cu_3SbSe_4. *Small Methods* **2024**, *8*, e2301377.

[42] Zhou, T.; Wang, L. J.; Zheng, S. Q.; Hong, M.; Fang, T.; Bai, P. P.; Chang, S. Y.; Cui, W. L.; Shi, X. L.; Zhao, H. Z. et al. Self-assembled 3D flower-like hierarchical Ti-doped Cu_3SbSe_4 microspheres with ultralow thermal conductivity and high *zT*. *Nano Energy* **2018**, *49*, 221–229.

[43] Bo, L.; Wang, Y. P.; Wang, W. Y.; Wang, L.; Li, F. J.; Zuo, M.; Ma, Y. Z.; Zhao, D. G. Grain size and compositional gradient dependence of thermoelectric performance for $Cu_{3-x}Ni_xSbSe_4$ materials. *Results Phys.* **2021**, *26*, 104337.

[44] Wang, B. Y.; Zheng, S. Q.; Chen, Y. X.; Wu, Y.; Li, J.; Ji, Z.; Mu, Y. N.; Wei, Z. B.; Liang, Q.; Liang, J. X. Band engineering for realizing large effective mass in Cu_3SbSe_4 by Sn/La codoping. *J. Phys. Chem. C* **2020**, *124*, 10336–10343.

[45] Wei, S. T.; Yu, L.; Zhang, Z. P.; Ji, Z.; Luo, S. T.; Liang, J. X.; Song, W. Y.; Zheng, S. Q. Enhancing the effective mass and covalent bond strength of Cu_3SbSe_4-based thermoelectric materials by Mn/Sn co-doping. *Mater. Today Phys.* **2023**, *38*, 101260.

[46] Scott, W.; Kench, J. R. Phase diagram and properties of Cu_3SbSe_4 and other $A_3^{I}B^{V}C_4^{VI}$ compounds. *Mater. Res. Bull.* **1973**, *8*, 1257–1267.

[47] Zhang, D.; Yang, J. Y.; Jiang, Q. H.; Zhou, Z. W.; Li, X.; Ren, Y. Y.; Xin, J. W.; Basit, A.; He, X.; Chu, W. J. et al. Simultaneous optimization of the overall thermoelectric properties of Cu_3SbSe_4 by band engineering and phonon blocking. *J. Alloys Compd.* **2017**, *724*, 597–602.

[48] Zhang, D.; Zhong, R. Q.; Gao, S. K.; Yang, L.; Xu, F.; He, P.; Liu, G. N.; San, X.; Yang, J. Y.; Luo, Y. B. et al. Reinforcing bond covalency for high thermoelectric performance in Cu_3SbSe_4-based thermoelectric material. *Sci. China Mater.* **2023**, *66*, 3644–3650.

[49] Liu, Y.; Calcabrini, M.; Yu, Y.; Genç, A.; Chang, C.; Costanzo, T.; Kleinhanns, T.; Lee, S.; Llorca, J.; Cojocaru-Mirédin, O. et al. The importance of surface adsorbates in solution-processed thermoelectric materials: The case of SnSe. *Adv. Mater.* **2021**, *33*, 2106858.

[50] Fiedler, C.; Calcabrini, M.; Liu, Y.; Ibáñez, M. Unveiling crucial chemical processing parameters influencing the performance of solution-processed inorganic thermoelectric materials. *Angew. Chem., Int. Ed.* **2024**, *63*, e202402628.

[51] McCarthy, C. L.; Webber, D. H.; Schueller, E. C.; Brutchey, R. L. Solution-phase conversion of bulk metal oxides to metal chalcogenides using a simple thiol-amine solvent mixture. *Angew. Chem. Int. Ed.* **2015**, *54*, 8378–8381.

[52] Ibáñez, M.; Hasler, R.; Genç, A.; Liu, Y.; Kuster, B.; Schuster, M.; Dobrozhan, O.; Cadavid, D.; Arbiol, J.; Cabot, A. et al. Ligand-mediated band engineering in bottom-up assembled SnTe nanocomposites for thermoelectric energy conversion. *J. Am. Chem. Soc.* **2019**, *141*, 8025–8029.

[53] Nes, E.; Ryum, N.; Hunderi, O. On the zener drag. *Acta Metall.* **1985**, *33*, 11–22.

[54] Manohar, P. A.; Ferry, M.; Chandra, T. Five decades of the zener equation. *ISIJ Int.* **1998**, *38*, 913–924.

[55] Liu, Y.; Calcabrini, M.; Yu, Y.; Lee, S.; Chang, C.; David, J.; Ghosh, T.; Spadaro, M. C.; Xie, C. Y.; Cojocaru-Mirédin, O. et al. Defect engineering in solution-processed polycrystalline SnSe leads to high thermoelectric performance. *ACS Nano* **2022**, *16*, 78–88.

[56] Fiedler, C.; Liu, Y.; Ibáñez, M. Solution-processed, surface-engineered, polycrystalline CdSe-SnSe exhibiting low thermal conductivity. *J. Vis. Exp.* **2024**, *207*, e66278.

[57] Liu, Y.; Lee, S.; Fiedler, C.; Chiara Spadaro, M.; Chang, C.; Li, M. Q.; Hong, M.; Arbiol, J.; Ibáñez, M. Enhancing thermoelectric performance of solution-processed polycrystalline SnSe with PbSe nanocrystals. *Chem. Eng. J.* **2024**, *490*, 151405.

[58] Chang, C.; Liu, Y.; Ho Lee, S.; Spadaro, M. C.; Koskela, K. M.; Kleinhanns, T.; Costanzo, T.; Arbiol, J.; Brutchey, R. L.; Ibáñez, M. Surface functionalization of surfactant-free particles: A strategy to tailor the properties of nanocomposites for enhanced thermoelectric performance. *Angew. Chem., Int. Ed.* **2022**, *61*, e202207002.

[59] Cadavid, D.; Wei, K. Y.; Liu, Y.; Zhang, Y.; Li, M. Y.; Genç, A.; Berestok, T.; Ibáñez, M.; Shavel, A.; Nolas, G. S. et al. Synthesis, bottom up assembly and thermoelectric properties of Sb-doped PbS nanocrystal building blocks. *Materials.* **2021**, *14*, 853.

[60] Dolzhnikov, D. S.; Zhang, H.; Jang, J.; Son, J. S.; Panthani, M. G.; Shibata, T.; Chattopadhyay, S.; Talapin, D. V. Composition-matched molecular "solders" for semiconductors. *Science* **2015**, *347*, 425–428.

[61] Lee, Y. K.; Luo, Z. Z.; Cho, S. P.; Kanatzidis, M. G.; Chung, I. Surface oxide removal for polycrystalline SnSe reveals near-single-crystal thermoelectric performance. *Joule* **2019**, *3*, 719–731.

[62] Zhou, C. J.; Lee, Y. K.; Yu, Y.; Byun, S.; Luo, Z. Z.; Lee, H.; Ge, B. Z.; Lee, Y. L.; Chen, X. Q.; Lee, J. Y. et al. Polycrystalline SnSe with a thermoelectric figure of mMerit greater than the single crystal. *Nat. Mater.* **2021**, *20*, 1378–1384.

[63] Liu, Y.; Li, M. Q.; Wan, S. H.; Lim, K. H.; Zhang, Y.; Li, M. Y.; Li, J. S.; Ibáñez, M.; Hong, M.; Cabot, A. Surface chemistry and band engineering in $AgSbSe_2$: Toward high thermoelectric performance. *ACS Nano* **2023**, *17*, 11923–11934.

[64] Snyder, G. J.; Snyder, A. H.; Wood, M.; Gurunathan, R.; Snyder, B. H.; Niu, C. N. Weighted mobility. *Adv. Mater.* **2020**, *32*, 2001537.

[65] Wang, B. Y.; Wang, Y. L.; Zheng, S. Q.; Liu, S. C.; Li, J.; Chang, S. Y.; An, T.; Sun, W. L.; Chen, Y. X. Improvement of thermoelectric properties of Cu_3SbSe_4 hierarchical with *in-situ* second phase synthesized by microwave-assisted solvothermal method. *J. Alloys Compd.* **2019**, *806*, 676–682.

[66] Wang, B. Y.; Zheng, S. Q.; Wang, Q.; Li, Z. L.; Li, J.; Zhang, Z. P.; Wu, Y.; Zhu, B. S.; Wang, S. Y.; Chen, Y. X. et al. Synergistic modulation of power factor and thermal conductivity in Cu_3SbSe_4 towards high thermoelectric performance. *Nano Energy* **2020**, *71*, 104658.

[67] Zhang, D.; Yang, J. Y.; Jiang, Q. H.; Fu, L. W.; Xiao, Y.; Luo, Y. B.; Zhou, Z. W. Improvement of thermoelectric properties of Cu_3SbSe_4 compound by In doping. *Mater. Des.* **2016**, *98*, 150–154.

[68] Li, D.; Li, R.; Qin, X. Y.; Zhang, J.; Song, C. J.; Wang, L.; Xin, H. X. Co-precipitation synthesis of Sn and/or S doped nanostructured $Cu_3Sb_{1-x}Sn_xSe_{4-y}S_y$ with a high thermoelectric performance. *CrystEngComm* **2013**, *15*, 7166–7170.

[69] Yang, C. Y.; Huang, F. Q.; Wu, L. M.; Xu, K. New stannite-like p-type thermoelectric material Cu_3SbSe_4. *J. Phys. D: Appl. Phys.* **2011**, *44*, 295404.

[70] Wang, W. Y.; Wang, Y. P.; Bo, L.; Wang, L.; Li, F. J.; Zuo, M.; Zhao, D. G. Enhanced thermoelectric properties of Cu_3SbSe_4 via compositing with nano-SnTe. *J. Alloys Compd.* **2021**, *878*, 160358.

[71] Zhao, L. J.; Yu, L. H.; Yang, J.; Wang, M. Y.; Shao, H. C.; Wang, J. L.; Shi, Z. Q.; Wan, N.; Hussain, S.; Qiao, G. J. et al. Enhancing

thermoelectric and mechanical properties of p-type Cu_3SbSe_4-based materials via embedding nanoscale Sb_2Se_3. *Mater. Chem. Phys.* **2022**, *292*, 126669.

[72] Zhang, D.; Yang, J. Y.; Bai, H. C.; Luo, Y. B.; Wang, B.; Hou, S. H.; Li, Z. L.; Wang, S. F. Significant average: *ZT* enhancement in Cu_3SbSe_4-based thermoelectric material via softening p-d hybridization. *J. Mater. Chem. A* **2019**, *7*, 17648–17654.

[73] Hong, M.; Chen, Z. G.; Yang, L.; Chasapis, T. C.; Kang, S. D.; Zou, Y. C.; Auchterlonie, G. J.; Kanatzidis, M. G.; Snyder, G. J.; Zou, J. Enhancing the thermoelectric performance of $SnSe_{1-x}Te_x$ nanoplates through band engineering. *J. Mater. Chem. A* **2017**, *5*, 10713–10721.

[74] Kim, H. S.; Gibbs, Z. M.; Tang, Y. L.; Wang, H.; Snyder, G. J. Characterization of lorenz number with Seebeck coefficient measurement. *APL Mater.* **2015**, *3*, 041506.

[75] Cahill, D. G.; Watson, S. K.; Pohl, R. O. Lower limit to the thermal conductivity of disordered crystals. *Phys. Rev. B* **1992**, *46*, 6131–6140.

[76] Zhang, Y. S.; Skoug, E.; Cain, J.; Ozoliņš, V.; Morelli, D.; Wolverton, C. First-principles description of anomalously low lattice thermal conductivity in thermoelectric Cu-Sb-Se ternary semiconductors. *Phys. Rev. B* **2012**, *85*, 054306.